Decoupling of a Disk Resonator From Linear Acceleration Via Mass Matrix Perturbation

David Schwartz
Postdoctoral Scholar
e-mail: daves@ucla.edu

Robert T. M'Closkey
Professor
e-mail: rtm@seas.ucla.edu

Department of Mechanical and
Aerospace Engineering,
University of California,
Los Angeles, CA 90095

Axisymmetric microelectromechanical (MEM) vibratory rate gyroscopes are designed so the central post which attaches the resonator to the sensor case is a nodal point of the two Coriolis-coupled modes that are exploited for angular rate sensing. This configuration eliminates any coupling of linear acceleration to these modes. When the gyro resonators are fabricated, however, small mass and stiffness asymmetries cause coupling of these modes to linear acceleration of the sensor case. In a resonator postfabrication step, this coupling can be reduced by altering the mass distribution on the resonator so that its center of mass is stationary while the operational modes vibrate. In this paper, a scale model of the disk resonator gyroscope (DRG) is used to develop and test methods that significantly reduce linear acceleration coupling. [DOI: 10.1115/1.4005275]

1 Introduction

High performance axisymmetric vibratory angular rate sensors have become a topic of great interest because of their potential to perform as well as ring laser gyroscopes while requiring much less power. The silicon disk resonator gyroscope (SiDRG), whose resonator is shown in Fig. 1, is being developed for tactical navigation applications (0.1 deg/h minimum bias instability) and motivates the study in this paper. These gyroscopes operate by utilizing the Coriolis coupling of in-plane modes to angular motion [1]. This paper focuses on the two elliptical Coriolis-coupled modes, also called the n = 2 modes, which are the pair of modes most widely used for angular rate sensing. Ideally, these Coriolis-coupled modes cannot be excited through linear acceleration of the sensor case. This theoretical "decoupling" from linear acceleration has two important benefits. First, it enables the resonators to achieve high quality factors by reducing coupling to the less lightly damped modes of the sensor case [2]. Second, it removes a source of spurious rate signals when the sensor is operated as a gyroscope since linear acceleration of the sensor case does not excite the modes.

No manufacturing process is perfect, however, and small mass and stiffness asymmetries are unavoidable. These asymmetries cause detuning of the modal frequencies in addition to coupling of the modes to linear acceleration. These two features can be seen in the frequency response plot in Fig. 1 in which the SiDRG's in-plane radial velocity is measured at its outermost ring while its central attachment point is given an in-plane excitation.

The problem of tuning the modal frequencies to degeneracy has been studied at great length for various axisymmetric resonators. Tuning has been achieved either by altering the resonator stiffness through, for example, electrostatic forces, or by altering the resonator mass distribution through mass deposition or removal [3–6]. The authors' recent paper described a method that uses the embedded drive and sense electrodes to guide a mass perturbation process for tuning resonators similar to the SiDRG [7].

Methods for decoupling the Coriolis-coupled modes from linear acceleration, however, have not been developed nearly as thoroughly as those for modal tuning. Zhbanov et al. analytically addressed the analogous decoupling problem in imperfect hemispherical resonators and proposed that the elimination of linear acceleration coupling to the n = 2 Coriolis-coupled modes can be achieved by causing the center of mass of the resonator to be a node of these modes [8]. The analysis showed that the coupling could be eliminated by "balancing" the first and third harmonics of the mass asymmetry.[1] The authors did not, however, explain how one would measure the mass asymmetry harmonics, nor has a reduction in linear acceleration coupling ever been empirically demonstrated in the open literature. The goal of this paper is to develop a method for experimentally determining the imbalance parameters associated with linear acceleration coupling and to demonstrate how these parameters can be used to effectively eliminate linear acceleration coupling.

The large scale resonator dubbed the macro disk resonator gyroscope (Macro DRG), which was previously used in the authors' tuning studies [7], is modified so that in-plane vibration of the center of the resonator is allowed. Thus, as the forcers drive the Coriolis-coupled modes, accelerometers attached to the central post measure the in-plane acceleration at the center of the resonator. The unperturbed resonator exhibits a clear response at the frequencies of the n = 2 Coriolis-coupled modes, which demonstrates coupling of the modes to vibration at the resonator's attachment point. As small magnets are placed on the outer rings of the resonator to implement reversible mass perturbations, a change can be seen in the nature of the linear acceleration coupling.

The discussion begins with an explanation of the process by which a coupling matrix, which includes the four "imbalance" parameters associated with linear acceleration coupling, can be extracted from multi-input/multi-output frequency response data. Experiments are then performed to show how the measured imbalance parameters change as the resonator is mass-loaded at different angular locations along the outer rings. The locations and magnitudes of the mass perturbations required for decoupling are then determined using the empirical relationship between mass placement and changes in the imbalance parameters. The final result shows a dramatic reduction in total linear acceleration coupling to the n = 2 Coriolis-coupled modes. A small increase in the quality factors of the modes is also observed.

Section 6 presents a general but systematic method for linear acceleration decoupling that uses only approximations of the first and third harmonics of the coupling data as its guide. By using the simplified model, this solution is implemented without detailed knowledge of the relationship between the perturbation locations and the change to the coupling matrix. This would likely be the most applicable method for decoupling typical axisymmetric resonators in a manufacturing environment.

---

[1]The first and third harmonics of the mass asymmetry are simply the first and third harmonics of the mass/unit length function along the equatorial axis of the hemispherical resonator. The harmonics are considered "balanced" when they have a value of zero. The analysis can be used to show that imbalances in the first and third harmonics of mass asymmetry are responsible for linear acceleration coupling in axisymmetric rings as well.
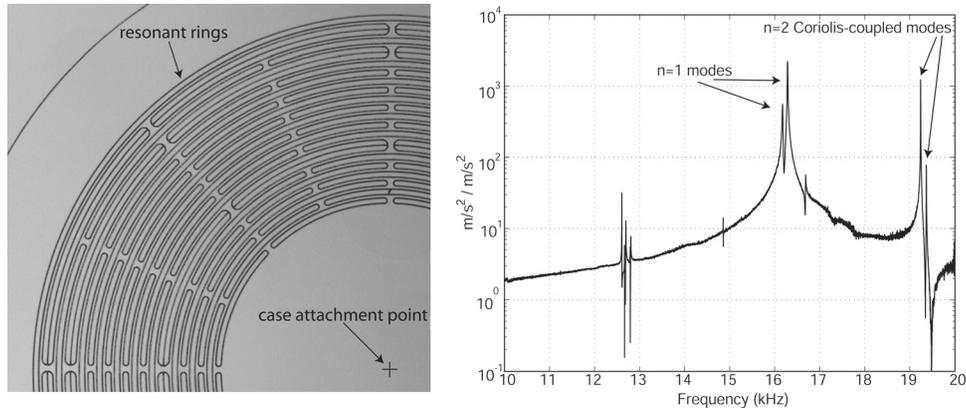
Fig. 1 Left: The Silicon Disk Resonator Gyroscope (SiDRG) has an 8 mm diameter and motivates the study in this paper. Only one quadrant of the resonant structure is shown here. In an operational gyroscope, electrodes are embedded between the rings to drive and sense the in-plane elliptical Coriolis-coupled modes. Right: The frequency response of the SiDRG exterior ring's radial velocity to in-plane excitation of the resonator's central attachment point. The two $n = 2$ Coriolis-coupled modes exist at two slightly different frequencies, indicating a detuning which is caused by small mass asymmetries. The fact that these modes are observable in this experiment suggests that the Coriolis-coupled modes exhibit coupling to movement at the attachment point, which can impact an operational gyroscope's performance by allowing linear case acceleration to produce spurious rate signals. By performing mass perturbations on the top surface of the resonator it is possible to reduce this coupling. This paper investigates methods for reducing the coupling and tests these methods on a macro-scale model of the SiDRG (shown in Fig. 2). The two $n = 1$ modes, which correspond to in-phase motion of the resonator rings, are nominally coupled to linear acceleration and Coriolis forces, but are not generally used for rate detection.

2 Experiment Description

The Macro DRG resonator is machined from 1018 grade, cold-rolled steel, and has an outer diameter of 11.6 cm and a mass of 187 g. The resonator thickness is 4.7 mm and each of its nineteen rings is 0.9 mm wide with 1.1 mm gaps between rings. Each ring is connected to its immediate neighbors by eight "spokes," with 45 deg angular spacing. The eight spokes connecting a ring to its outer neighbor, however, are rotated by 22.5 deg from the eight spokes connecting the ring to its inner neighbor. Thus, the positions of the eight spokes alternate radially between positions 22.5 deg from each other giving sixteen angular spoke locations, as can be seen in Fig. 2. The resonator is attached at its center to a 1.2 cm diameter aluminum post that is suspended 19 cm below the location where the post is clamped. Small NdFeB magnets, each with a 1.6 mm diameter, 0.8 mm thickness and mass of approximately 12 mg, can be attached to the top surface of the resonator to create reversible localized mass perturbations.

Actuation and sensing of the resonator are achieved using electromagnetic actuators and capacitive sensing pick-offs. A photograph of the experiment along with a diagram of the layout is shown in Fig. 2 and block diagrams are shown in Fig. 3. Each electromagnet is a modified relay that uses variable current through its solenoid to exert a radial magnetic force on the resonator. Each sensing pick-off consists of a 5 mm diameter electrode placed parallel to the outside edge of the outermost ring of the resonator. The resonator is biased at 60 V and, as the resonator vibrates, the capacitance between the resonator and the electrode changes. Charge on the electrode flows to the virtual ground of the transimpedance amplifier which is configured with a 1 MΩ feedback resistor, thereby providing a gain of 10^6 V/A.

Sensing of the post motion is achieved with two accelerometers that are mounted onto a nylon sheath near the post's attachment to the resonator. The nylon electrically isolates the accelerometers from the resonator bias. The accelerometer measurements are AC
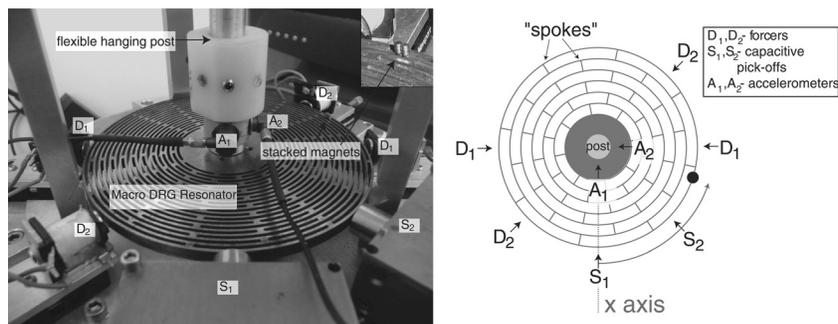
Fig. 2 Left: The experimental setup of the Macro DRG, configured to measure linear acceleration coupling. The resonator hangs from the flexible post so that in-plane movement of the resonator's attachment point can be measured by the accelerometers. On the right hand side of the resonator, near one of the D_2 actuators, two stacks of the NdFeB magnets can be seen. These are used to create a reversible mass perturbation to the resonator. Right: A schematic of the forcer/pickoff arrangement for the Macro DRG. The angular positions for mass perturbations are measured as the angle with respect to the x-axis, which is aligned with the A_1 and S_1 sensors and intersects the central axis of the post.
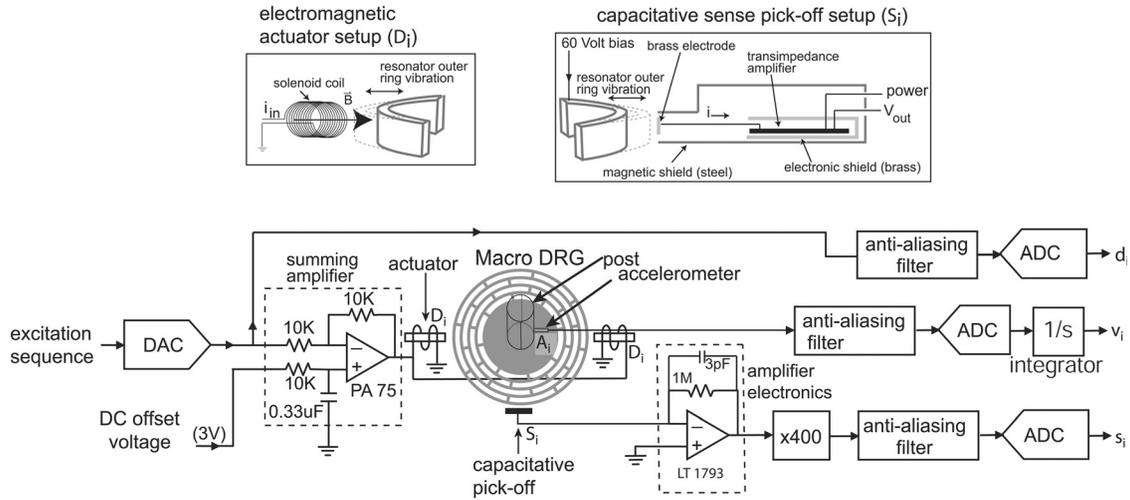
Fig. 3 Top: Electromagnetic actuator and capacitive sensor setup. Bottom: Testing block diagram.

coupled and then integrated so that they are proportional to the post velocity in a neighborhood of the $n = 2$ Coriolis modes. The A_1 accelerometer is placed so that its sense axis is parallel to the sensing axis of S_1, and the A_2 accelerometer is placed so that its sense axis is 90 deg counter-clockwise from the A_1 accelerometer. The locations of the sensors and actuators are shown in the right hand illustration in Fig. 2. Each drive signal is applied to opposing paired electromagnetic actuators so that the net force applied to the entire resonator is minimized. The second pair of actuators is placed 45 deg from the first so that they present "orthogonal" excitations with respect to the $n = 2$ Coriolis-coupled modes. Finally, a pick-off is placed 90 deg from each electromagnetic actuator so that the two pick-offs are 45 deg apart (in a likewise "orthogonal" arrangement). The x-axis in Fig. 2 acts as a reference for angular locations on the resonator.

The two 2×2 frequency responses of the Macro DRG with no magnets added are shown in Fig. 4. A 10 s chirp signal in a neighborhood of the $n = 2$ Coriolis-coupled modes is used to drive the actuators, which yields frequency response estimates with a 0.1 Hz resolution.

3 Empirical Estimation of the Coupling Matrix

The linear acceleration coupling model that relates the two frequency responses displayed in Fig. 4 assumes that the vibration of the resonator couples to the velocity of the post by the coupling matrix, $\overline{B}$, i.e.,

$$\begin{bmatrix} v_1 \\ v_2 \end{bmatrix} = \overline{B} \begin{bmatrix} s_1 \\ s_2 \end{bmatrix}, \quad \overline{B} \in \mathbb{R}^{2\times2} \tag{1}$$

where s_1 and s_2 are the radial velocities of resonator at S_1 and S_2 while v_1 and v_2 are the velocities of the structure at A_1 and A_2. The bar over the coupling matrix denotes that it is constant with respect to frequency.

The radial velocities can be thought of as measurements of the "velocity" states of the Coriolis modes and, because $\overline{B}$ is a real matrix, v_1 and v_2 are simply linear combinations of these states. The coupling matrix, $\overline{B}$, is generally identified for a particular mass perturbation scenario and can be represented as

$$\overline{B} = \overline{B}_0 + \sum_{i=1}^{N} \Delta\overline{B}(m_i, \phi_i), \quad \overline{B}_0, \Delta\overline{B}(m_i, \phi_i) \in \mathbb{R}^{2\times2} \tag{2}$$

where $\overline{B}_0$ is the coupling matrix for the nominal resonator and $\Delta\overline{B}(m_i, \phi_i)$ is the change in the coupling matrix for each individual mass perturbation of mass m_i at location ϕ_i. For this paper, the

angle ϕ is the counter-clockwise angle from the x-axis of that perturbation, as illustrated in Fig. 2. This model is partially inspired by the analytical model of the effects of mass perturbations on a simple ring as discussed later in Sec. 4.2.

The experimental setup enables the measurement of a complex-valued 2×2 transfer function, $B(\omega)$ (Fig. 5). This coupling transfer function is defined by

$$B(\omega) = H_v(\omega)H_s^{-1}(\omega)$$

$$\text{where } H_s(\omega) = \begin{bmatrix} \dfrac{s_1}{d_1}(\omega) & \dfrac{s_1}{d_2}(\omega) \\ \dfrac{s_2}{d_1}(\omega) & \dfrac{s_2}{d_2}(\omega) \end{bmatrix} \in \mathbb{C}^{2\times2} \text{ and}$$

$$H_v(\omega) = \begin{bmatrix} \dfrac{v_1}{d_1}(\omega) & \dfrac{v_1}{d_2}(\omega) \\ \dfrac{v_2}{d_1}(\omega) & \dfrac{v_2}{d_2}(\omega) \end{bmatrix} \in \mathbb{C}^{2\times2} \tag{3}$$
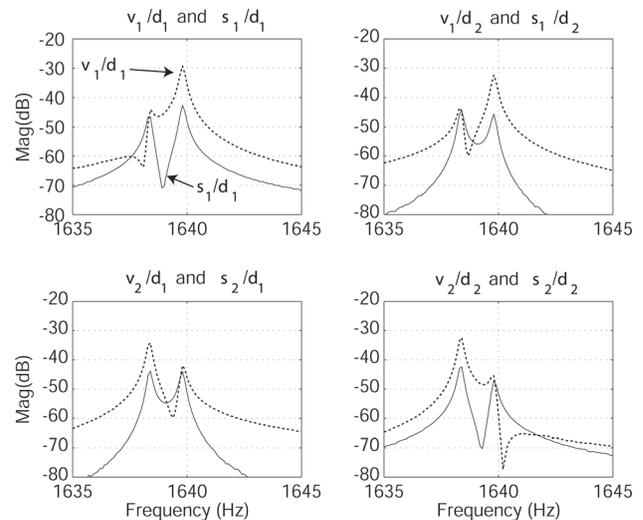
Fig. 4 The 2×2 frequency response of the accelerometer velocity to a chirp input from each forcer, denoted H_v, is displayed using the dotted traces, while the frequency response of the capacitive sense measurements from the same inputs, denoted H_s, is displayed using the solid traces. If no linear acceleration coupling were present, the accelerometer velocity responses would be nearly linear in this frequency range and correspond to motion of resonator center as a consequence of the cantilever response of the post to which it is attached.
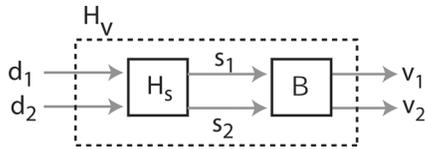
Fig. 5 Block diagram for identification of the coupling matrix, $B(\omega)$, from measured responses H_v and H_s

Fig. 7 An experiment that tests the linearity of $\Delta\overline{B}$ with respect to m. Five separate tests were done in which the value of $\overline{B}$ was measured as magnets were added to an individual spoke. Magnets were attached in two stacks so that the final test with twelve magnets is performed with two stacks of six magnets. The average of the four channels of $\Delta\overline{B}$ is plotted as the dots whereas the error bars give the standard deviation of the tests. The solid line is a least square fit to the averaged data. The assumption that $\Delta\overline{B}$ is linear with respect to m appears to be appropriate.

The real and imaginary parts of a sample measurement of $B(\omega)$ are shown in Fig. 6. In order to agree with (1), $B(\omega)$ should be real and constant with respect to frequency in a neighborhood of the Coriolis-coupled modes. In this experiment, however, the small imaginary part and the small slope are caused by the dynamics of the post. These dynamics are linear with respect to frequency in the narrow frequency range of the Coriolis-coupled modes, but change as mass perturbations are made to the structure. Because it is difficult to compensate for the effect of the post, each of the four components of the real, 2×2 coupling matrix, $\overline{B}$, are approximated by averaging the corresponding real parts of $B(\omega)$, denoted below as $B_{\mathbb{R}}(\omega)$, at the frequencies of the two Coriolis-coupled modes, i.e.,

$$\overline{B} = \frac{1}{2}(B_{\mathbb{R}}(\omega_1) + B_{\mathbb{R}}(\omega_2)) \tag{4}$$

where ω_1 and ω_2 are the two frequencies of the $n = 2$ Coriolis-coupled modes.

4 A Model for Mass Perturbation Effects on the Coupling Matrix

4.1 Empirical Derivation of a Coupling Model. An experiment was conducted to measure $\Delta\overline{B}(m, \phi)$, which is the change in the linear acceleration coupling matrix $\overline{B}$ of the Macro DRG for a single mass perturbation. Although it is possible to quantify the effects of mass perturbations performed on different rings, in this experiment, all perturbations are constrained to the ring with the second largest radius. The first part of the experiment tests the linearity of m in the $\Delta\overline{B}$ function. A measurement of $\overline{B}$ was taken each time an additional magnet was added to the spoke 11.25 deg counter-clockwise from the x-axis (i.e., $\phi = 11.25$) and the difference between the measured perturbed coupling matrix and the unperturbed one, denoted $\overline{B}_0$ in Eq. (2), was computed. The experiment was conducted five times in order to assess the repeatability

of the results. The mean and standard deviation of the results are shown in Fig. 7. The data closely follow a least squares linear fit, confirming that $\Delta\overline{B}$ is adequately linear with respect to m.

In the second part of the experiment, each mass perturbation consisted of six small magnets (i.e., $m = 72$ mg when using 12 mg magnets) placed at various angular locations, ϕ_i. The matrix $\overline{B}$ was then measured for each case when the perturbation was applied to the sixteen spokes as well as the sixteen midpoints between the spokes. The differences between each measured coupling matrix, $\overline{B}$, and the unperturbed one, $\overline{B}_0$, are shown in Fig. 8. The experiment was conducted five times and the plots show the mean and standard deviation of the results.

An expression for relationship between the coupling matrix and mass placement is found using a discrete Fourier transform (DFT). The formula for the DFT for this case is

Fig. 6 The real (left) and imaginary (right) parts of the four components of $B(\omega)$. The slopes of the real parts and the small imaginary parts are caused by post dynamics in the region of the modes of interest. A constant, real coupling matrix, $\overline{B}$, is calculated by taking the average of the real parts of $B(\omega)$ at the two resonant frequencies.
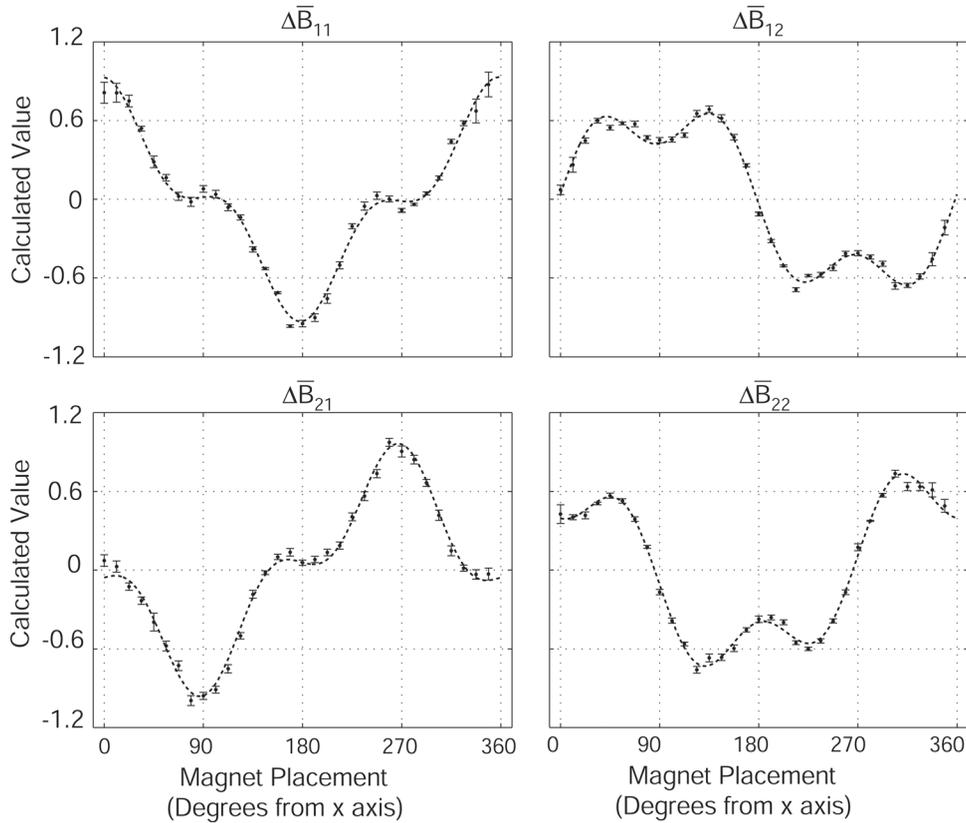
Fig. 8 The four components of the perturbation matrix, $\Delta\overline{B}$, plotted against the placement of the perturbing mass. In this case, the coupling matrix, $\overline{B}$, was measured as a six magnet test mass is placed at each of the spokes as well as the midpoints in between the spokes. The perturbation matrix is taken as the difference between the coupling matrix of the perturbed resonator and coupling matrix associated with the unperturbed resonator. The test was conducted five times and the error bars represent the standard deviation of the data. The dotted trace is given by the first and third harmonic approximation of the averaged data explicitly given in Eq. (6).

$$X_{pq}^{(k)} = \sum_{l=0}^{31} \Delta\overline{B}_{pq}^{AVE}(6\,m_0, \phi_{l+1}) e^{-j\frac{2\pi}{32}lk}$$

$$k = 0, \dots, 31 \text{ for } p, q = 1, 2$$

(5)

where m_0 is the mass of one magnet (approximately 12 mg), which is the smallest mass perturbation that can be applied to the Macro DRG. The superscript (k) on $X_{pq}^{(k)}$ denotes that it is

the kth component of the vector X_{pq}, the superscript AVE above $\Delta\overline{B}$ denotes that it is the averaged value for that value of ϕ_{l+1} and $j = \sqrt{-1}$. The DFT factors the original functions into a weighted sum of harmonics. The magnitudes of the first sixteen harmonics are shown in Fig. 9. The approximation of the linear acceleration perturbation function that uses only $X_{pq}^{(1)}$ and $X_{pq}^{(3)}$ $(p, q = 1, 2)$ is

$$\Delta\overline{B}(m, \phi) \approx m \begin{bmatrix} 1.39\cos(\phi + 0.014) + 0.53\cos(3\phi + 0.096) & 1.35\sin(\phi + 0.015) + 0.51\sin(3\phi + 0.116) \\ -1.41\sin(\phi + 0.125) + 0.58\sin(3\phi + 0.101) & 1.34\cos(\phi + 0.174) - 0.54\cos(3\phi - 0.034) \end{bmatrix}$$

(6)

where m is the magnitude of the mass perturbation in milligrams and the argument terms are expressed in radians. This approximation fits the data well, and is plotted as the dotted trace in Fig. 8.

4.2 Comparison to the Analytical Ring Model. The prominent features of the *empirically* derived perturbation function for the Macro DRG are, perhaps unsurprisingly, similar to the features of the *analytically* derived perturbation functions for similar, but simpler, structures. The analysis of Zhbanov et al., which addresses hemispherical resonators, suggests that linear acceleration coupling can be eliminated by balancing only the first and third harmonics of the angular mass distribution [8]. The same analytical technique can be applied to a single ring

to reach the same conclusion. As the disk resonator structure is essentially a collection of rings, it is instructive to derive the effect of mass perturbations on linear acceleration coupling in planar rings.

First, the center of mass is expressed in terms of its x and y components, denoted C_x and C_y, respectively. Next these are decomposed into static and dynamic parts such that

$$C_x = C_{x0} + C_x' \frac{\sin\omega t}{2\left(m_{ring} + \sum_{i=1}^{N} m_i\right)} \quad \text{and}$$

$$C_y = C_{y0} + C_y' \frac{\sin\omega t}{2\left(m_{ring} + \sum_{i=1}^{N} m_i\right)}$$

(7)
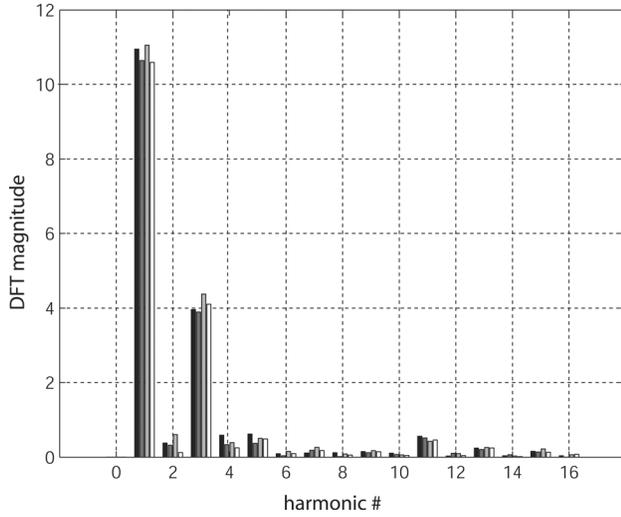
Fig. 9 The magnitudes of the discrete Fourier transform of the mean values plotted in Fig. 8. The four bars of each grouping are the $\Delta\overline{B}_{11}$, $\Delta\overline{B}_{12}$, $\Delta\overline{B}_{21}$, and $\Delta\overline{B}_{22}$ components, respectively. It is clear that the first and third harmonics are the dominant features of the perturbation function.

where ω is the frequency of vibration, m_{ring} is the total mass of the symmetric part of the ring and N is the number of discrete masses, m_i, which cause the deviation from symmetry.[2] By applying the mode shape of the n = 2 Coriolis-coupled modes,[3] the dynamic parts of the center of mass position can be written as

$$
C_x' = A\cos(2\psi)\sum_{i=1}^{N} m_i[3\cos\phi_i + \cos 3\phi_i]
$$
$$
+ A\sin(2\psi)\sum_{i=1}^{N} m_i[3\sin\phi_i + \sin 3\phi_i]
$$
$$
C_y' = A\cos(2\psi)\sum_{i=1}^{N} m_i[-3\sin\phi_i + \sin 3\phi_i]
$$
$$
+ A\sin(2\psi)\sum_{i=1}^{N} m_i[3\cos\phi_i - \cos 3\phi_i]
$$
(8)

where ψ is the angle between the modal axes and the x-axis, A is the amplitude of vibration, and the N total masses have angular positions ϕ_i, as illustrated in Fig. 10. One can express this relationship using a coupling matrix for a ring, $\overline{B}_{\text{ring}}$, that has the same form as Eq. (1)

$$
\begin{bmatrix} C_x' \\ C_y' \end{bmatrix} = \overline{B}_{\text{ring}} \begin{bmatrix} A\cos(2\psi) \\ A\sin(2\psi) \end{bmatrix} \text{ where}
$$
$$
\overline{B}_{\text{ring}} = \begin{bmatrix} \sum_i m_i[3\cos\phi_i + \cos 3\phi_i] & \sum_i m_i[3\sin\phi_i + \sin 3\phi_i] \\ \sum_i m_i[-3\sin\phi_i + \sin 3\phi_i] & \sum_i m_i[3\cos\phi_i - \cos 3\phi_i] \end{bmatrix}
$$
(9)

This equation reveals that, in theory, linear acceleration coupling is only caused by mass distributions with nonzero first and third harmonics. Next, the change in $\overline{B}_{\text{ring}}$ for a single mass perturbation is defined as

---

[2]The denominators of Eq. (7) are factored out of the dynamic parts because the total deviation from symmetry, $\sum m_i$, is much smaller than the total mass of the resonator, meaning that that the inverse of the denominators are effectively constant with respect to the mass asymmetry.

[3]The mode shape used in this derivation is defined by $w(\phi, t) = 2A\cos(2\phi - 2\Psi)\sin(\omega t)$ and $u(\phi, t) = A\sin(2\phi - 2\Psi)\sin(\omega t)$ where w and u are the radial and tangential parts of the velocity of a point on the ring at angular position ϕ [9]. An exaggerated mode shape is visualized as the dotted ellipse in Fig. 10.
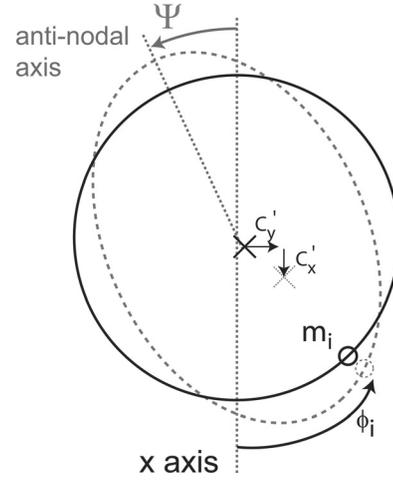
Fig. 10 Basic diagram for ring linear acceleration coupling analysis. The dotted shape represents a possible mode shape for the ring, with antinodal axis an angle Ψ from the x-axis. The position of the single attached mass, m_i, oscillates with the ring, thereby causing the center of mass, shown here as '×', to oscillate as well.

$$
\Delta\overline{B}_{\text{ring}}(m, \phi) = m\begin{bmatrix} 3\cos\phi + \cos 3\phi & 3\sin\phi + \sin 3\phi \\ -3\sin\phi + \sin 3\phi & 3\cos\phi - \cos 3\phi \end{bmatrix}
$$
(10)

Note that the signals s_1 and s_2 in the experimental model given in Eq. (1) would act as measurements for $A\cos(2\Psi)$ and $A\sin(2\Psi)$ if the resonator were a simple ring. Indeed, it has been shown that the mode shape of n = 2 Coriolis-coupled modes for the Macro DRG deviates only slightly from that of a simple ring [7]. Thus, it is not surprising that this analytical model for the perturbation function of a ring and the experimentally derived model for the Macro DRG given in Eq. (6) share important characteristics. Namely, the perturbation relationships of both are linear with respect to m and are dominated by the first and third harmonics with respect to ϕ.

5 Decoupling Using the Experimental Perturbation Function

The experimental model is ultimately validated by its usefulness in driving each of the elements of $\overline{B}$ to zero. Thus, the decoupling problem is stated as finding the combination of N masses, m_i, placed at positions ϕ_i, such that

$$
\overline{B} + \sum_{i=1}^{N} \Delta\overline{B}(m_i, \phi_i) = \mathbf{0}
$$
(11)

The decoupling method discussed in this section, dubbed the "spokes method," restricts angular locations of the perturbations to the locations of the spokes. The spokes are logical locations for adding mass because the perturbation results from the previous section were measured at the spokes. Using the approximation that $\Delta\overline{B}(m, \phi)$ is linear in m, one only needs to choose four locations, $\Phi = \{\phi_1, \phi_2, \phi_3, \text{ and } \phi_4\}$, so that a solution $\mathbf{M} = [M_1 \quad M_2 \quad M_3 \quad M_4]^\mathsf{T}$ exists to $\mathbf{A}(\Phi)\mathbf{M} = \mathbf{b}$ where

$$
\mathbf{A}(\Phi) = \begin{bmatrix} \Delta\overline{B}_{11}(m_0,\phi_1) & \Delta\overline{B}_{11}(m_0,\phi_2) & \Delta\overline{B}_{11}(m_0,\phi_3) & \Delta\overline{B}_{11}(m_0,\phi_4) \\ \Delta\overline{B}_{12}(m_0,\phi_1) & \Delta\overline{B}_{12}(m_0,\phi_2) & \Delta\overline{B}_{12}(m_0,\phi_3) & \Delta\overline{B}_{12}(m_0,\phi_4) \\ \Delta\overline{B}_{21}(m_0,\phi_1) & \Delta\overline{B}_{21}(m_0,\phi_2) & \Delta\overline{B}_{21}(m_0,\phi_3) & \Delta\overline{B}_{21}(m_0,\phi_4) \\ \Delta\overline{B}_{22}(m_0,\phi_1) & \Delta\overline{B}_{22}(m_0,\phi_2) & \Delta\overline{B}_{22}(m_0,\phi_3) & \Delta\overline{B}_{22}(m_0,\phi_4) \end{bmatrix},
$$
$$
\text{and } \mathbf{b} = \begin{bmatrix} -\overline{B}_{11} \\ -\overline{B}_{12} \\ -\overline{B}_{21} \\ -\overline{B}_{22} \end{bmatrix}
$$
(12)

Table 1 Linear acceleration decoupling using the spokes method

	$\|H_v\|_2(\sqrt{Hz}m/s/V)$	Optimization solution								Added number of magnets for next perturbation			
		Angular locations (deg)				Number of magnets							
First step	192.9	191.25,	213.75,	258.75,	281.25	7.0,	13.3,	5.3,	4.4,	7,	13,	5,	4
Iteration 1	67.2	33.75,	146.25,	168.75,	281.25	3.3,	1.0,	0.9,	3.0	3,	1,	1,	3
Iteration 2	8.1	11.25,	123.78,	236.25,	348.75	0.1,	0.4,	0.1,	0.4	0,	0,	0,	0
										Total magnets added			
										37			

Again, m_0 is the mass of one magnet so that M_1, M_2, M_3, and M_4 are the number of magnets necessary for each of the four perturbations. A solution can be chosen from the many possible ones by minimizing the total perturbation mass required

$$\min_{\phi_1,\phi_2,\phi_3,\phi_4} \sum_{i=1}^{4} M_i$$

$$\text{subject to: } \mathbf{A}(\Phi)\mathbf{M} = \mathbf{b} \qquad (13)$$

$$\det(\mathbf{A}) \neq 0$$

$$\phi_i \in \phi_{\text{spokes}}, M_i \geq 0, \quad i = 1, 2, 3, 4$$

in which the $M_i \geq 0$ constraint is in place because mass cannot be removed in this scenario. The requirement that $\mathbf{A}$ is nonsingular eliminates the values of Φ for which the corresponding $\mathbf{M}$ is not unique while not disqualifying any minimizing solutions. Note that the values of $\Delta\overline{B}$ used here are simply the average values of $\Delta\overline{B}$ as plotted in Fig. 8. The optimization is performed by determining $\mathbf{M}$ for each of the 1820 possible values of Φ. The optimal Φ and $\mathbf{M}$ are chosen as those that minimize cost function, $\sum_{i=1}^{4} M_i$. Generally, the optimal values of M_i are not integers even though the actual perturbations require whole numbers of magnets. Thus, the values of M_i are rounded after the optimization.

The coupling matrix derived from the data in Fig. 6 is used to start the decoupling process which can be followed in Table 1. At each step, optimization (13) suggests that perturbations of M_i magnets be added to the locations ϕ_i. The actual number of magnets utilized for each perturbation is calculated by rounding to the nearest integral value. A new coupling matrix is estimated and the process is repeated until the optimization suggests that each of the optimal perturbations is less than 0.6 magnets. The linear acceleration coupling is assessed by computing the H_2 norm of the forcer/accelerometer transfer function in a neighborhood of the $n = 2$ modes. This is discussed in more detail in Sec. 5.1.

5.1 Quantifying Coupling Reduction. The exact and approximated values of the H_2 norm of H_v in the frequency band $[f_1, f_2]$ are given by

$$\|H_v\|_2^2 = \int_{f_1}^{f_2} \text{tr}(H_v^*(f)H_v(f))df$$

$$\approx \sum_{k=0}^{N} \text{tr}(H_v^*(f_1 + k\Delta_f)H_v(f_1 + k\Delta_f))\Delta_f$$

where $\text{tr}(\cdot)$ is the trace of a matrix and H_v^* is the conjugate transpose of H_v. The H_2 norm is a natural choice because it facilitates the calculation of the root-mean-square acceleration to a white-noise force disturbance applied to the $n = 2$ modes. More specifically, if independent band-limited white-noise inputs of intensity $\gamma \frac{V}{\sqrt{Hz}}$ are applied to the electromagnetic actuators, the root-mean-square output of the accelerometers is given by $\gamma \| H_v \|_2$. The approximated value of $\| H_v \|_2$ is tracked throughout the linear acceleration decoupling process using $f_1 = 1620$ Hz, $f_2 = 1660$ Hz, $N = 400$, and $\Delta_f = 0.1$ Hz. The final value $\| H_2 \|_2$ is less than 5% of the initial value, confirming that there is a significant reduction in coupling. The value of $\text{tr}(H_v^*H_v)$ is plotted versus frequency in Fig. 11 prior to and after decoupling. The reduction in coupling is also qualitatively confirmed in Fig. 12, which displays the accelerometer outputs when uncorrelated band-limited white-noise signals drive the electromagnetic forcers before and after decoupling. Figure 13 displays the power spectrum before and after decoupling, averaged over 20 such tests.

Another effect of linear acceleration coupling is that the quality factors of the Coriolis-coupled modes of the resonator are reduced because energy is transferred from these modes to the more heavily damped post. These quality factors can be extracted in a ring
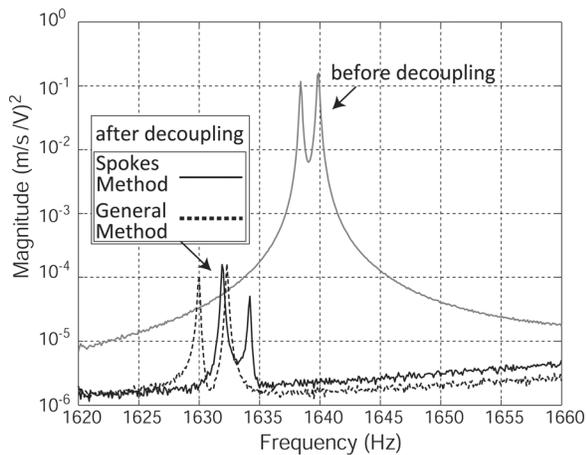
Fig. 11 A plot of $\text{tr}(H_v^*H_v)$ before and after the two decoupling methods were implemented. Each of the methods exhibit over a 95% reduction in the H_2 norm of the forcers-to-accelerometers transfer functions. For reference, the transfer function H_v measured prior to decoupling is the solid trace plotted in Fig. 4.
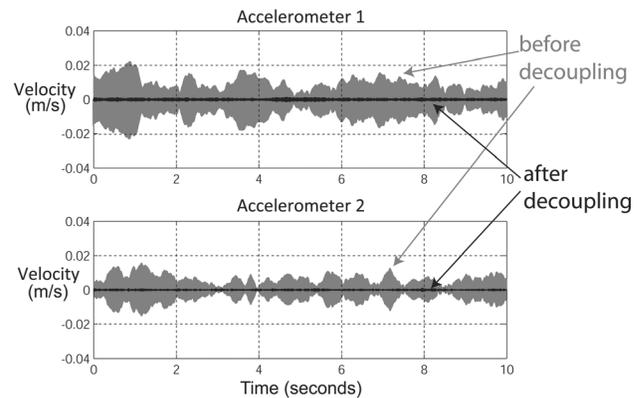
Fig. 12 Uncorrelated white-noise inputs with equal variance are applied to the two electromagnetic forcers in a frequency band encompassing the modes of interest for both the original and decoupled cases. The velocities of the post are measured before decoupling (gray) and after decoupling (black) using the spokes method.
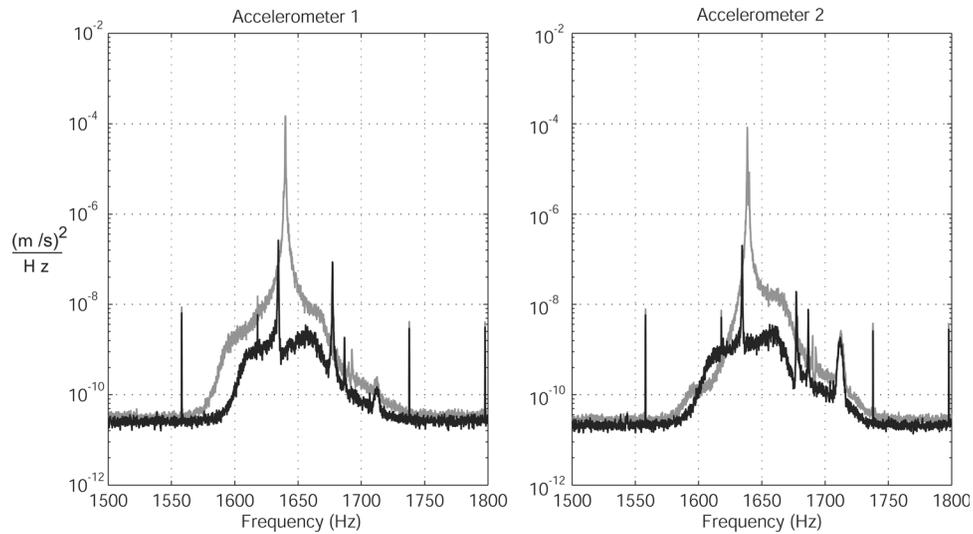
Fig. 13 The averaged power spectrum of both accelerometers with uncorrelated band-limited noise inputs with a $50\text{mv}/\sqrt{\text{Hz}}$ spectral density before (gray) and after (black) decoupling is performed using the spokes method. The modes of interest are located between 1630 and 1650 Hz.

down test by exciting a single mode and then observing the decay rates after the excitation is removed. Figure 14 displays the filtered peak amplitude of the output during ring down tests performed before and after decoupling. The quality factor of the low frequency mode increases from 6.8 K to about 7.8 K after decoupling while the quality factor of the high frequency mode increases from 7.9 K to about 8.0 K.

6 Decoupling Without Initial Measurement of the Perturbation Function

The linear acceleration decoupling process discussed in Sec. 5 works very well for the resonator under test and demonstrates the feasibility of reducing linear acceleration coupling through mass perturbations. This section presents a more generalized and robust method. The first improvement removes the need for a previously measured perturbation function. This consider-

ably increases the appeal of the method because, when other resonators are fabricated, the perturbation functions will likely be different. The Spokes Method, which, as implemented in the previous section, requires that sixteen irreversible perturbations be made to the resonator in order to derive its perturbation function and clearly involves more testing than necessary. In contrast, the method discussed in this section, denoted the "general method," approximates the first and third harmonics of the perturbation function with as few perturbations as possible and then updates the perturbation function as more data sets are acquired. The second improvement over the previous method removes the constraint that perturbations only be made at the spokes. By allowing perturbations to take place at any angular location the optimal perturbation requires fewer masses. Also, this allows the process to be generalized to ring-shaped resonators that do not have strongly preferred perturbation locations.
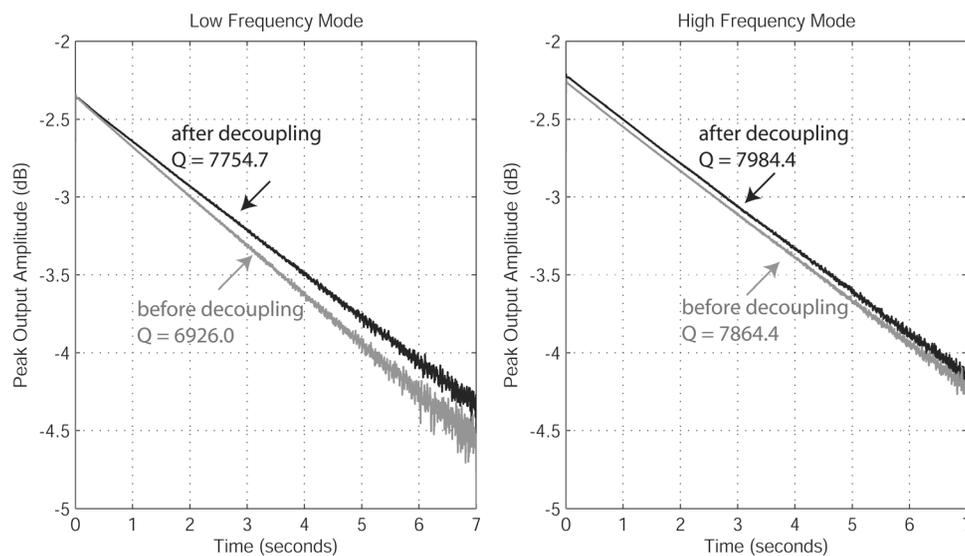
Fig. 14 A ring down test is performed on the resonator before and after decoupling is implemented and the time responses of the peak outputs are plotted. The quality factors are approximated by the slope of linear least square fits to the data. The low frequency mode shows a marked increase in its quality factor.

6.1 Online Approximation of the Perturbation Function. For the present approach, the perturbation function uses only the first and third harmonics so that each component can be expressed as

$$\Delta\overline{B}(m_i, \phi_i)_{pq} = m_i\Big(\mathbf{x}_{pq}^{(1)}\cos\phi + \mathbf{x}_{pq}^{(2)}\sin\phi \\ + \mathbf{x}_{pq}^{(3)}\cos 3\phi + \mathbf{x}_{pq}^{(4)}\sin 3\phi\Big) \tag{14}$$

where $\mathbf{x}_{pq}$ is the vector of the weightings on the cosine and sine terms of the first and third harmonics for $\Delta\overline{B}(m_i, \phi_i)_{pq}$. With $N \geq 4$ calibration measurements of $\Delta\overline{B}$, the perturbation function can be estimated by finding the least squares solution of

$$\begin{bmatrix} m_1\cos(\phi_1) & m_1\sin(\phi_1) & m_1\cos(3\phi_1) & m_1\sin(3\phi_1) \\ m_2\cos(\phi_2) & m_2\sin(\phi_2) & m_2\cos(3\phi_2) & m_2\sin(3\phi_2) \\ \vdots & \vdots & \vdots & \vdots \\ m_N\cos(\phi_N) & m_N\sin(\phi_N) & m_N\cos(3\phi_N) & m_N\sin(3\phi_N) \end{bmatrix}$$

$$\mathbf{x}_{pq} = \begin{bmatrix} \Delta\overline{B}_{pq}(m_1, \phi_1) \\ \Delta\overline{B}_{pq}(m_2, \phi_2) \\ \vdots \\ \Delta\overline{B}_{pq}(m_N, \phi_N) \end{bmatrix} \tag{15}$$

for $p, q = 1, 2$. A notable feature of this method is that perturbations of greater magnitude have a greater influence on the approximation of the perturbation function.

6.2 Solution to the General Decoupling Problem. The two harmonic perturbation function, built using Eq. (14), can now be used to find solutions to (11) in which $\phi_i \in [0, 2\pi]$. The minimization, Eq. (13), is generalized to

$$\min_{\phi_1, \phi_2, \phi_3, \phi_4} \sum_{i=1}^{4} M_i$$
$$\text{subject to: } \mathbf{A}(\Phi)\mathbf{M} = \mathbf{b} \tag{16}$$
$$\det(\mathbf{A}) \neq 0$$
$$\phi_i \in [0, 2\pi), M_i \geq 0, \quad i = 1, 2, 3, 4$$

in which the spoke constraint has been removed and $\mathbf{A}$ and $\mathbf{b}$ are defined as in Eq. (12) using the two harmonic perturbation function, $\Delta\overline{B}(m_i, \phi_i)$, from Eq. (14). Though the problem is not quasi-convex, the steepest descent method appears to converge to the global minimal solution when the solution to Eq. (13) is used as an initial condition. The minimizing result is at the edge of the feasible region, meaning that the difference between two of the optimal angular locations is arbitrarily small (causing $\mathbf{A}$ to be

nearly singular) and/or one of the optimal mass magnitudes is arbitrarily close to zero. Thus, at least one of the masses is redundant and the solution actually requires only two or three point masses. A brief discussion comparing this solution to those found in the literature is contained in the Appendix.

6.3 Choice of Initial Perturbation Locations. The general method must start with an estimate of the perturbation function. Thus, four "calibrating" perturbations are made to provide this estimate. Ideally, these perturbations are performed in a way that allows for a balanced estimate of the perturbation function while not adding additional coupling to the system. In order to ensure that an equal emphasis is placed on the first and third harmonics, the four test masses of equal magnitude should be spaced using the following relation

$$\phi_1 = \phi_2 - \pi/4 \pmod{\pi}$$
$$= \phi_3 - \pi/2 \pmod{\pi} \tag{17}$$
$$= \phi_4 - 3\pi/4 \pmod{\pi}$$

This constraint guarantees that the condition number of left hand matrix of Eq. (15) is 1 when $N = 4$ and $m_1 = m_2 = m_3 = m_4$. Thus, an error in any individual measurement of $\Delta\overline{B}_{pq}$ will not disproportionately corrupt the approximation of $\mathbf{x}_{pq}$. In practice, this constraint forces the perturbation locations to be no closer than 45 deg apart.

One may choose any four locations that satisfy restraint (17), though, it is advantageous to choose locations that also reduce coupling. Though crude, the perturbation function for an axisymmetric ring generally approximates the perturbation function for any axisymmetric device. Thus, this function is used to guide the first step. One chooses locations that best reduce the imbalance parameters by solving

$$\min_{\phi_1, \phi_2, \phi_3, \phi_4} \Bigg[\sum_{i=1}^{4} 3\cos\phi_i + \cos 3\phi_i, \quad \sum_{i=1}^{4} 3\sin\phi_i + \sin 3\phi_i, \\ \sum_{i=1}^{4} -3\sin\phi_i + \sin 3\phi_i, \quad \sum_{i=1}^{4} 3\cos\phi_i - \cos 3\phi_i \Bigg] \mathbf{b}$$
$$\text{subject to: } \phi_i \in \phi_{\text{spokes}} \text{ and } \phi_i \text{ satisfies (17) for } i = 1, 2, 3, 4 \tag{18}$$

where $\mathbf{b}$ is defined as in Eq. (12). The $\phi_i \in \phi_{\text{spokes}}$ restraint is added here to simplify the minimization. Unlike optimizations (13) and (16), which theoretically determine the locations and magnitudes of perturbations that eliminate coupling, optimization (18) theoretically determines the locations that will cause the greatest reduction in coupling for fixed perturbation magnitudes.

6.4 Implementation of the General Method. The techniques developed in Secs. 6.1–6.3 are used to guide the General

Table 2 Linear acceleration decoupling using the general decoupling method

| | | Optimization solution | | | | | | | Added number of magnets for next perturbation | | | |
	$\|H_v\|_2 (\sqrt{Hz}m/s/V)$	Angular locations (deg)				Number of magnets						
Calibration 1	192.9	56.25,	101.25,	146.25,	191.25	NA			2,	2,	2,	2
Calibration 2	195.9	234.45,			299.16	19.96,		14.59	4,			4
Calibration 3	163.3	336.93,	96.92,		216.9	6.7,	0.43,	28.90	6,	0,		6
Calibration 4	140.5	187.0,			260.35	12.5,		12.0	8,			8
Iteration 1	44.5	165.8,			234.2	3.47,		4.09	3,			4
Iteration 2	11.9	58.9,	179.9,		299.9	0.541,	0.8371,	0.33	0,	1,		0
End	10.6	50.41,			312.2	0.54,		0.31	0,			0
									Total magnets added			
									52			
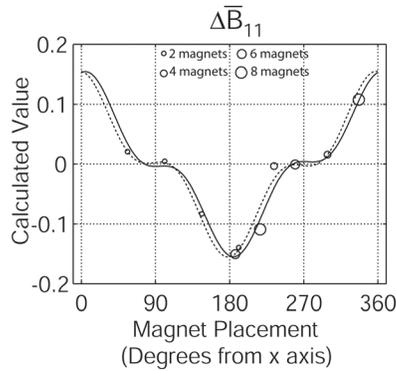
Fig. 15 A plot of the (1, 1) component of $\Delta\overline{B}(\mathbf{m_0}, \varphi)$ as measured during the calibrations for the example of the general method. The diameters of the circles scale with the magnitudes of the perturbation used for each calibration step. The first and third harmonic approximation of the perturbation function, $[\cos\varphi \ \sin\varphi \ \cos 3\varphi \ \sin 3\varphi]\mathbf{x_{11}}$, is plotted using the solid line. This approximation is used to guide the final two decoupling steps. The dotted line is the first and third harmonic approximation that was shown in Fig. 8. Though it does not precisely match the previous approximation, which utilized more perturbations, the new approximation is still a useful decoupling tool.

Method, the steps of which can be followed in Table 2. For this implementation, two magnets were used at each of the four calibration points in the first step, and the change in the coupling matrix is measured for each calibration mass added. Despite attempting to add the masses in a way that reduces coupling, it appears $\|H_v\|_2$ increased slightly. The unexpected increase demonstrates a potential pitfall of putting too much faith in an analytically defined perturbation function (in this case $\Delta B_{ring}(m, \phi)$).

For the next step, two more calibration masses, made up of four magnets each, are placed at the two locations suggested by optimization (16). For cases in which three masses are suggested, the calibration masses are simply placed at the two points requiring the most mass. The measurements are used to re-estimate $\mathbf{x_{11}}$, $\mathbf{x_{12}}$, $\mathbf{x_{21}}$, and $\mathbf{x_{22}}$. The third and fourth calibration steps use six and eight magnets, respectively, and the estimate of the two harmonic perturbation function achieves greater accuracy. A plot of one channel of the estimated perturbation function can be seen in Fig. 15. The last two steps use the refined model to guide the placement of the last few magnets. The process is terminated when all suggested mass perturbations are less than 0.6 magnets. The value of $\mathrm{tr}(H_v^* H_v)$ is plotted versus frequency in Fig. 11 so the result can be compared to the result using the Spokes Method. Again, the coupling is reduced by a large degree. The general method did, however, require more magnets than the spokes method. This can be attributed to the use of a less accurate perturbation function and the addition of magnets that were required for the initial calibration.

7 Conclusions

Axisymmetric resonators are ideal structures for creating vibratory gyroscopes, however, manufacturing imperfections inevitably couple the modes that are exploited for angular rate sensing to linear acceleration of the sensor's case. A systematic approach to reduce the coupling has been proposed and is suitable for planar microelectromechanical (MEM) resonators in which strategic mass loading or removal can be implemented. The process was demonstrated on a macroscale resonator (the Macro DRG) that, by virtue of its size, facilitated the numerous experiments that were conducted in order to empirically determine the nature of the acceleration coupling. Using the Macro DRG allowed us to focus on developing a decoupling process without the challenges posed by working with MEM devices. Despite the fact that the experimental apparatus is limited by the quantized nature of the mass

perturbations imposed by the minimum magnet size, the results show that a factor of 20 reduction in coupling is easily achievable. Although the Macro DRG is considerably more complicated than the ring structures typically addressed in the literature, the empirically measured Macro DRG linear acceleration coupling perturbation function closely follows the analytical ring resonator model. Nevertheless, the proposed approach is based on measuring the perturbation function for each resonator with a systematic sequence of experiments.

Acknowledgment

Appendix: A Comparison To Literature

The basic problem of decoupling using a known perturbation function, articulated in Eq. (11), can be reformulated as

$$\begin{bmatrix} \sum_{i=1}^{N} m_i \cos(\phi_i) \\ \sum_{i=1}^{N} m_i \sin(\phi_i) \\ \sum_{i=1}^{N} m_i \cos(3\phi_i) \\ \sum_{i=1}^{N} m_i \sin(3\phi_i) \end{bmatrix} = \begin{bmatrix} \mathbf{x}_{11}^{T} \\ \mathbf{x}_{12}^{T} \\ \mathbf{x}_{21}^{T} \\ \mathbf{x}_{22}^{T} \end{bmatrix}^{-1} \mathbf{b} \qquad (A1)$$

by combining Eqs. (11) and (14). This formulation more clearly demonstrates that the problem is equivalent to the harmonic balancing problems solved by Fox et al. and Zhbanov et al. [8,10]. Fox's method, formulated for problems involving even harmonics, produces two mass solutions when they exist, and these solutions agree with the end result of optimization (16) in these cases. When the solution requires three masses, however, Fox's method does not give a solution. For example, if the right hand side of Eq. (A1) equates to $[0\ 0\ 1\ 0]^{T}$, then, three masses are required for decoupling. Zhbanov's method is complete and simple, but requires four masses, and generally requires more mass than the solution to optimization (16). The results to optimization (16) are expressed in a well-posed manner in Ref. [11], but have been excluded here for brevity.

References

[1] Lynch, D. D., 1988, "Coriolis Vibratory Gyros," Symposium Gyro Technology, Stuttgart, Germany.
[2] Lynch, D. D., 1984, "Hemispherical Resonator Gyro," R. R. Ragan, ed., *Inertial Technology for the Future*, IEEE Transactions on Aerospace Electronic Systems, Vol. AES-20, No. 4, pp. 414–444.
[3] Kim, D. J., and M'Closkey, R. T., 2006, "A Systematic Method for Tuning the Dynamics of Electrostatically Actuated Vibratory Gyros," IEEE Trans. Control Syst. Technol., **14**(1), pp. 69–81.
[4] Gallacher, B. J., 2000, "Multi-Modal Tuning of a Ring Gyroscope Using Laser Ablation," Proc. Inst. Mech. Eng. C., **217**, pp. 557–576.
[5] Rourke, A. K., McWilliam, S., and Fox, C. H. J., 2002, "Multi-Mode Trimming of Imperfect Thin Rings Using Masses at Pre-Selected Locations," J. Sound Vib., **256**(2), pp. 319–345.
[6] Fell, C. P., 1996, "Method for Matching Vibration Mode Frequencies on a Vibrating Structure," U.S. Patent No. 5,739,410.
[7] Schwartz, D., Kim, D. J., and M'Closkey, R. T., 2009 "Frequency Tuning of a Disk Resonator Gyro Via Mass Matrix Perturbation," ASME J. Dyn. Syst., Meas., Control, **131**(6), 061004.
[8] Zhbanov, Y. K., and Zhuravlev, V. F., 1998, "On the Balancing of a Hemispherical Resonator Gyro," Mech. Solids, **33**(4), pp. 2–13.
[9] Allaei, D., Soedel W., and Yang, T. Y., 1986, "Natural Frequencies of Rings That Depart From Perfect Axial Symmetry," J. Sound Vib., **111**, pp. 9–27.
[10] Rourke, A. K., McWilliam, S., and Fox, C. H. J., 2001, "Multi-Mode Trimming of Imperfect Rings," J. Sound Vib., **248**(4), pp. 695–724.
[11] Schwartz, D., 2010, "Mass Perturbation Techniques for Tuning and Decoupling of a Disk Resonator Gyroscope," Ph.D. thesis, University of California, Los Angeles, CA.